

Wavelength selection in the crown splash

Li V. Zhang,¹ Philippe Brunet,² Jens Eggers,³ and Robert D. Deegan^{1,a)}

¹*Department of Physics and Center for the Study of Complex Systems, University of Michigan, Ann Arbor, Michigan 48109, USA*

²*Institut d'Electronique de Microelectronique et de Nanotechnologies, UMR CNRS 8520, Avenue Poincaré, 59652 Villeneuve d'Ascq, France*

³*Department of Mathematics, University of Bristol, Bristol BS8 1TW, United Kingdom*

(Received 11 September 2009; accepted 19 November 2010; published online 22 December 2010)

The impact of a drop onto a liquid layer produces a splash that results from the ejection and dissolution of one or more liquid sheets, which expand radially from the point of impact. In the crown splash parameter regime, secondary droplets appear at fairly regularly spaced intervals along the rim of the sheet. By performing many experiments for the same parameter values, we measure the spectrum of small-amplitude perturbations growing on the rim. We show that for a range of parameters in the crown splash regime, the generation of secondary droplets results from a Rayleigh–Plateau instability of the rim, whose shape is almost cylindrical. In our theoretical calculation, we include the time dependence of the base state. The remaining irregularity of the pattern is explained by the finite width of the Rayleigh–Plateau dispersion relation. Alternative mechanisms, such as the Rayleigh–Taylor instability, can be excluded for the experimental parameters of our study. © 2010 American Institute of Physics. [doi:10.1063/1.3526743]

I. INTRODUCTION

The impact of a drop with a thin film of the same liquid produces a spray of secondary droplets that results from the emission, expansion, and breakup of one or more sheetlike jets. Splashes are essential to diverse physical processes and applications such as gas transfer across the air–sea interface,¹ cooling,² coatings,³ and combustion.⁴ The spatial pattern and size distribution of secondary droplets are in general highly complex,⁵ vary qualitatively with experimental conditions,^{6,7} and have yet to be understood.⁸

Figure 1 shows the end stage of a crown splash in which the rim of a sheetlike jet breaks into secondary droplets distributed almost uniformly along its perimeter. The name of the splash derives from the resemblance of this final stage to a crown with equally spaced tines, as exemplified in Edgerton's iconic photograph *Milk Coronet*.⁹ The events culminating in a crown splash begin with a smooth cylindrical sheetlike jet extending outward and upward. The leading edge of this jet (i.e., the rim) is pulled by surface tension toward the sheet,^{10,11} and grows in diameter as it entrains fluid from the sheet. Next, the rim develops a symmetry-breaking corrugation, and in a much later nonlinear phase of the original instability, the rim's crests sharpen into jets which pinch off to form secondary droplets.

Due to the high speed and small scale structure of a splash there are few quantitative time-resolved observations of crown formation.^{12–22} This is true in particular for the earliest stages of the growth of the rim, during which perturbations of the rim are extremely small. Basic questions regarding the origin and evolution of splashes remain unanswered.⁸ Foremost among these is: what mechanism leads to the generation of secondary droplets?

From the earliest investigations, the leading suspect for the mechanism responsible for secondary droplets was the Rayleigh–Plateau instability,²³ which causes cylindrical jets to break into droplets. Worthington²⁴ experimented with tori of mercury on a solid surface to address this question, but was unable to directly compare the number of ejected droplets with Plateau's theory. Yarin and Weiss¹⁴ cast doubt on the relevance of this mechanism based on timescale arguments, and noted that there is a discrepancy between the expected and measured number of ejected droplets. Fullana and Zaleski²⁵ argued that the Rayleigh–Plateau instability is slowed prohibitively by the increase of the rim's radius with time. Rieber and Frohn²⁶ found support for the Rayleigh–Plateau mechanism in computer simulations but only for large initial perturbations. Bremond and Villermaux²⁷ analyzed rim instabilities for the lamella produced by impacting jets, and found the Rayleigh–Plateau instability to be the dominant mechanism.

Mechanisms other than Rayleigh–Plateau have been suggested for the generation of secondary droplets. Yarin and Weiss¹⁴ proposed a nonlinear amplification mechanism. Gueyffier and Zaleski²⁸ argued for the Richtmyer–Meshkov instability. Krechetnikov and Homsy²² argued for a combination of the Richtmyer–Meshkov and Rayleigh–Taylor instability.

We think there are two reasons why the symmetry breaking instability of a splash has been interpreted in so many, seemingly contradictory ways. First, depending on parameters, there exist many different splash morphologies,⁵ which may result from different instabilities. Second, there is a lack of quantitative experimental data that characterizes both the symmetry breaking as well as the base state on which the instability grows. Here we focus on a parameter regime in which the crown splash grows from an initially smooth sheet

^{a)}Electronic mail: rddeegan@umich.edu.

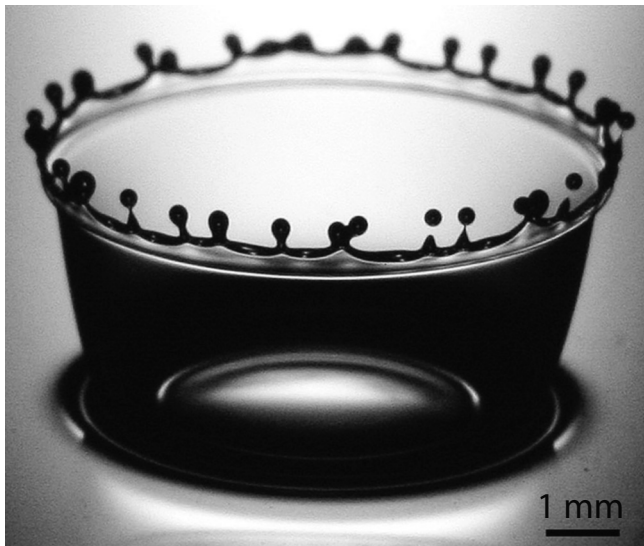


FIG. 1. Crown splash (silicone oil: $Re=966$, $We=874$, $H^*=0.2$).

formed on impact into a thin layer of the same fluid at moderate speed. We image the instability that appears on the leading edge of the ejected sheet at multiple times onward from $\approx 100 \mu\text{s}$ after impact for multiple impact speeds and layer depths. From our images we extract the spectrum of the instability, and compare this to the various mechanisms that are cited in the literature. Our results for peak position and width of the spectrum are in excellent agreement with Rayleigh–Plateau mechanism.

The paper is formatted as follows. Section II describes our experimental setup and procedures. Section III A describes our observations of the morphology of splashes. We show that highly regular crown splashes in thin layers occur only for low Reynolds number. Section III B describes our experimental measurements of the instability spectra from still images of the rim's corrugation. For the majority of experiments the spectra at any given time after impact were produced from a single image; for our most precise experiments we averaged over ten spectra obtained at equal times. Section IV describes a comparison of our data with a calculation based on the Rayleigh–Plateau instability. For our most precise measurements with averaged spectra the measured and calculated peak wavelengths agree within 5%. Section V describes a comparison of our experiments with other proposed mechanism such as Rayleigh–Taylor and Richtmyer–Meshkov. Our measurements exclude these mechanisms. Section VI discusses and summarizes our results in the context of other splashing studies.

II. EXPERIMENTAL METHODS

Our experiments identified the parametric regime for crown splashes and measured the evolution of these splashes. A 10 cm diameter $\lambda/10$ glass optical flat, coated with an indium-tin oxide film to prevent the destabilization of the thin liquid films due static charge build up, was placed in a 15×15 cm container with a glass bottom. Fluid was added to the container until the optical flat was submersed, forming a film of height h above the optical flat, as shown in Fig. 2.

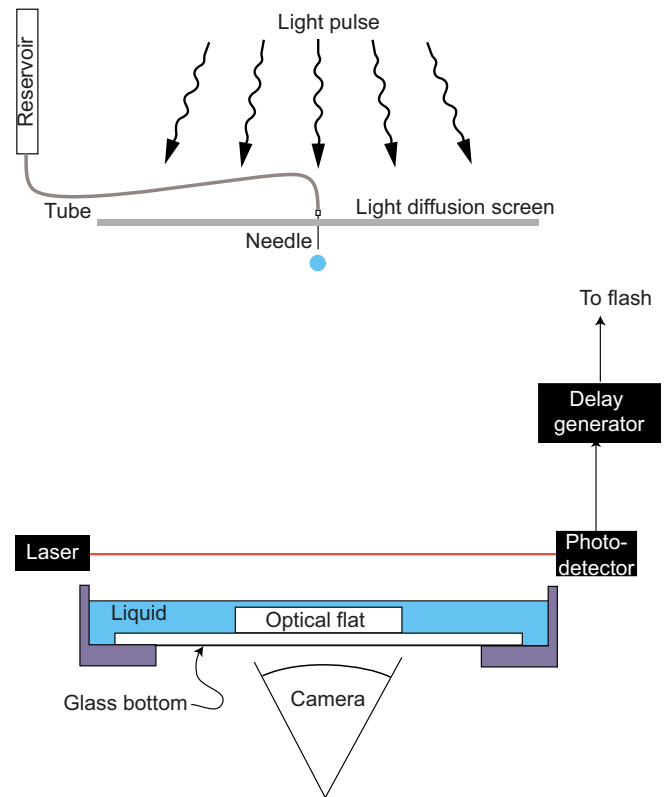


FIG. 2. (Color online) Apparatus for observing the evolution of crown splashes. A drop forms and detaches from a hypodermic needle held a fixed height above a thin layer of the same liquid. The needle is gravity fed from a reservoir. As the drop falls toward the liquid layer, it interrupts a laser sheet focused onto a photodetector which initiates a countdown on a delay generator. After a preprogrammed time, the delay generator fires a flash onto a diffusion screen, and a back-lit image of the impact event is recorded from below through the transparent substrate or from the side.

The orientation of the container was then adjusted so that the flat lay parallel to the fluid's surface to within 3×10^{-4} rad. The depth of the layer was varied between 100 and 400 μm depending on the experiment. A single drop of diameter D was released from a gravity fed 30 gauge hypodermic needle at fixed height above the liquid layer. The interval between drops was longer than 10 s, which ensured that the liquid layer fully relaxed between impact events. The drop struck the liquid layer with a velocity U normal to the surface.

The dimensionless parameters for describing droplet impact in the absence of a surrounding gas are the Weber number $We=(\rho DU^2/\gamma)$, the Reynolds number $Re=(DU/\nu)$, the Froude number $Fr=(U^2/gD)$, and the dimensionless fluid depth $H^*=h/D$, where g is the acceleration due to gravity, and ρ , γ , ν are the density, surface tension, and kinematic viscosity of the fluid, respectively. Past studies ignored the ambient gas and gravity on the basis that densities and viscosities of liquids are much higher those of the gas, and that the timescale for gravitational effects is long compared to the duration of a splash. We follow this practice here, and concentrate on the We , Re , and H^* . Nonetheless, we note that the recent work of Xu *et al.*²⁹ found a significant influence of the ambient air on drop impact on a *dry* solid. We believe the effect of air to be much weaker in our experiment, since there is no moving contact line.

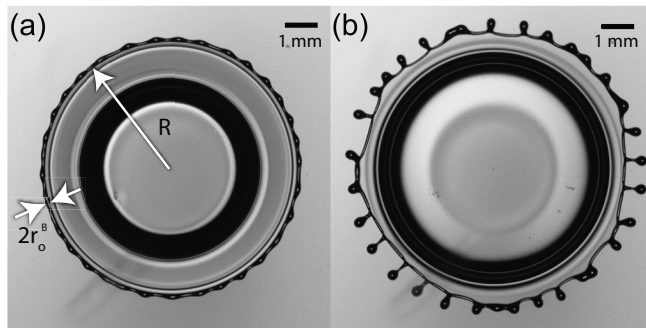


FIG. 3. Crown splash ($Re=894$, $We=722$, $H^*=0.1$) from below at $t=1.85$ ms and $t=3.15$ ms after impact showing the one-to-one correspondence between instability wavelength and the number of droplets. The arrows define rim radius as seen from below r_o^B and rim's radial distance from the impact center R .

Our data on the morphology of splashes were obtained with a high speed camera (Phantom 5.0 or 7.3) viewing the impact from the side. Our data on the evolution of the rim were obtained from images simultaneously recorded through the glass substrates and from the side using digital cameras (Nikon D80 with a 90 mm $f/2.8$ macro and Canon 20D with a 100 mm $f/2.8$ macro lens) and a single 600 ns, 6 J pulse from a spark flash (Palfash 501, Pulse Photonics Ltd.). The flash was triggered after a preprogrammed delay interval initiated by the drop cutting a laser sheet focused onto a photodiode. The triggering event was reproducible to within ± 5 μ s. By varying the delay time, the evolution of the impact was recreated from a composite of still images. Examples of typical bottom and side images are shown in Figs. 3 and 4. The virtue of this technique is that it produces much higher spatial and temporal resolution than can be achieved



FIG. 4. (left) Images illustrating the crown sheet at 250 and 2100 μ s after impact. (right) Cartoon of sheet cross-section. At early times, the leading edge of the sheet is almost horizontal. The shape changes as the rim retracts relative to the fluid (though still moving away from the center in the laboratory frame) and entrains the fluid in the sheet. Eventually the entire flat portion of the sheet is entrained in the rim. The kink in the late time sheet is a wave generated when the rim reaches the vertical section of the sheet. Scale bar equals 2 mm.

TABLE I. Parameters for experiments. In all case the fluid was a silicone oil.

Parameter set number	We	Re	H^*	Liquid (cSt)	Speed (cm/s)	Radius (cm)	Layer depth (μ m)
1	760	1060	0.20	5	308	0.172	350
2	1015	1266	0.20	5	344	0.184	360
3	813	1133	0.10	5	308	0.184	184
4	1043	642	0.20	10	349	0.184	368
5	607	979	0.19	5	266	0.184	350
6	824	1141	0.15	5	310	0.184	275

with existing high speed video cameras. The speed of the drop at impact was measured with the high speed video camera.

Our measurements of the crown splash were performed with a 5 cSt ($\rho=0.918$ g/cm³, $\gamma=19.7$ dynes/cm) or 10 cSt ($\rho=0.935$ g/cm³, $\gamma=20.6$ dynes/cm) silicone oil purchased from Clearco. Our experiments were performed for the parameters listed in Table I.

For each parameter set we took data at least every 100 μ s after the rim emerges from beneath the drop, prior to which the rim is not visible. For parameter set number 1 ($Re=1060$, $We=760$, $H^*=0.20$) we collected much more data than in other parameter sets in order to reduce fluctuations.

III. EXPERIMENTAL RESULTS

A. Splash morphologies

By observing splashes for a range of Weber and Reynolds numbers and fixed $H^*=0.2$, we classified the morphologies. The parametric dependence of these morphologies is shown in Fig. 5. Crown splashes appear only in the regime labeled *crown droplets*. A regular crown is also observed in the parameter range below this regime, but these crowns do

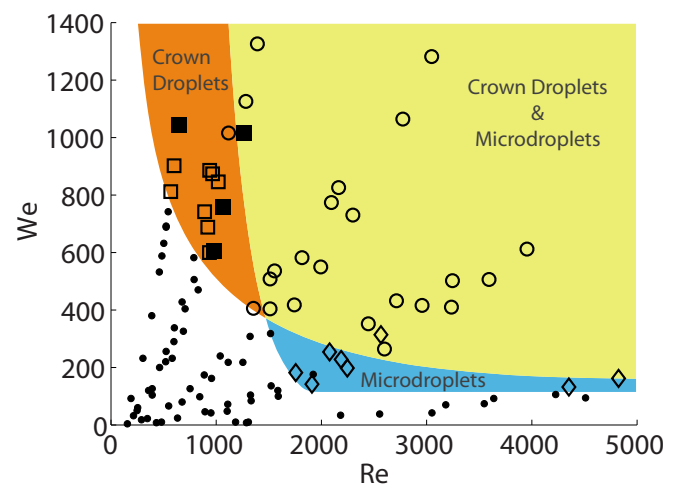


FIG. 5. (Color online) Qualitative character of impact for $H^*=0.2$. No splash (black small circles), crown droplets with (open circles) and without (squares) microdroplets, and microdroplets without crown droplets (diamonds). The filled squares indicate the parameter set for all experiments at $H^*=0.2$ reported here. Spatially periodic crown splashes form exclusively in the crown droplets regime.

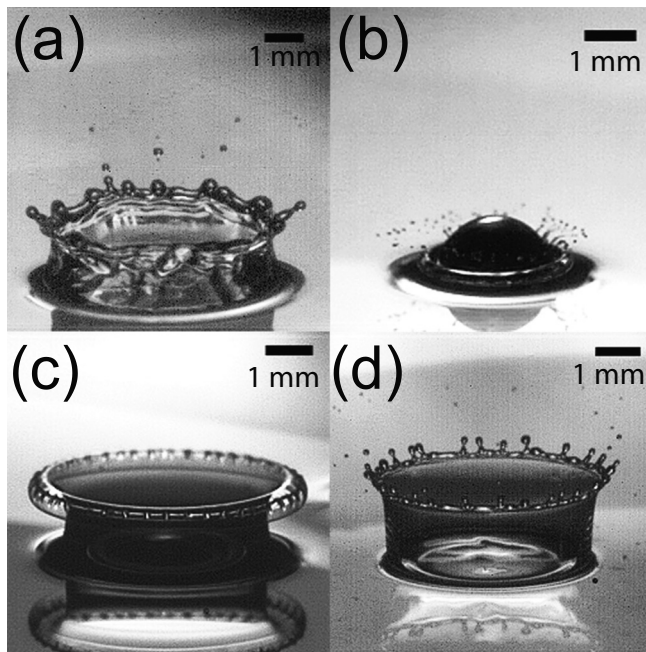


FIG. 6. Morphologies of splashes outside of the crown splash regime: (a) water ($Re=6044$, $We=254$, $H^*=0.2$) produces a highly irregular crown sheet and splash, (b) glycerol/water mixture ($Re=2566$, $We=314$, $H^*=0.2$) produces droplets immediately upon impact, long before the crown sheet forms, (c) silicone oil ($Re=1392$, $We=1266$, $H^*=0.2$) produces a trapped torus of air, and (d) isopropanol for $Re=1354$, $We=406$, $H^*=0.2$ produces a wavy crown sheet and continuously ejects droplets as the crown grows upward.

not form secondary droplets because the growth of the corrugation pattern is slower and thus the sheet retraction occurs before droplets can pinch-off. Outside of this domain, splashes are more irregular and complicated⁵ as shown by the examples in Fig. 6.

B. Crown splashes

From our bottom-view images we extract the corrugation of the outer edge of the splash to within $\pm 6 \mu\text{m}$. A selection of these data are shown in Fig. 7. For each parameter set, we capture this corrugation every $100 \mu\text{s}$ and compute the power spectrum of these data. From the spectra, we extracted the peak wavelength (i.e., the most energetic mode) by fitting the peak to a Gaussian. For parameter set number 1, we capture the edge profile with much greater time resolution (up to every $10 \mu\text{s}$ during the first $700 \mu\text{s}$) and in addition repeated the measurement at $500 \mu\text{s}$ intervals ten times. From the latter data, we computed the spectrum for each image, and averaged these results to arrive at the spectra shown in Fig. 8. The peaks of these spectra, obtained by fitting the upper parts of the peaks to a Gaussian, are plotted in Fig. 11. The data from the inner edge yield the same spectra but with a reduced amplitude due to the fact that the rim is angled away from the vertical and we only observe its projection on to the horizontal plane.

As shown in Figs. 7 and 8, the peak wavelength shifts to larger values for later times, corresponding to a coarsening of the corrugation. Furthermore, the corrugation does not grow evenly at all points on the rim, but rather nucleates at several

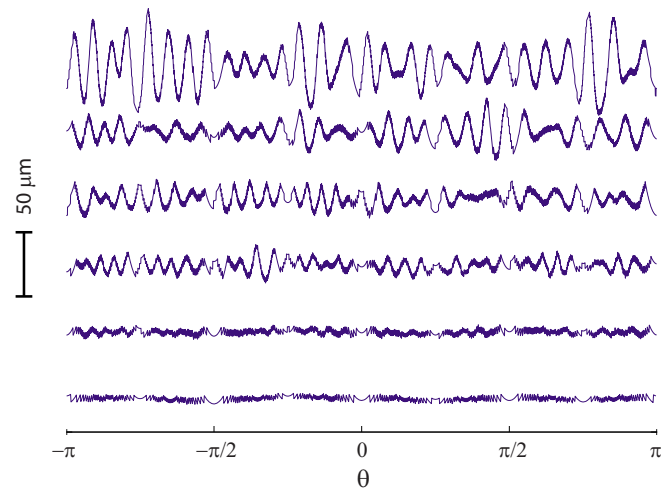


FIG. 7. (Color online) Profiles of the outer rim corrugation at successive times (from bottom to top: 115, 365, 605, 1105, 1605, and 2085 μs after impact), starting from a smooth profile and growing to a highly corrugated state. Note that the corrugation nucleates at different places and these domains merge at later times. The noise on the early time profiles are digitization artifacts: the camera pixel size is $6.0 \mu\text{m}$.

locations. These domains grow and merge, consistent with the growth of the unstable modes from random noise. At later times each corrugation sharpens and begins to form a droplet, as demonstrated by the example in Fig. 3. The number of corrugations, and hence the number of proto-droplets, is set by the ratio of the rim circumference to the peak wavelength. The actual number of emitted droplets is smaller because of mergers between adjacent incipient droplets. Therefore, the number of secondary droplets is bounded from above by the most unstable wavelength of the instability.

From our bottom-view images, we also extracted the average radius of the rim as seen from below r_o^B , and the horizontal distance of the centerline of the rim from the impact center R . We processed the images to extract the position of the inner and outer edges of the rim. The radii of the inner r_{inner} and outer r_{outer} edge were determined by fitting to a circle, and from these we obtained the rim radius $r_o^B = \frac{1}{2}(r_{\text{outer}} - r_{\text{inner}})$ and the radial position of the rim $R(t) = \frac{1}{2}(r_{\text{outer}} + r_{\text{inner}})$. Figure 3 illustrates the physical features corresponding to these parameters, and Fig. 10 shows their time dependence for parameter set number 1.

From our side-view images, we measured the average radius of the rim as seen from the side r_o^S . Measurements were only possible over a short segment of the rim because of the shallow depth of field of our optical system, and were difficult to obtain due to the small changes in the impact position which would move the rim out of the depth of field. These data are shown by the squares in Fig. 10. Our side view is to good approximation orthogonal to the bottom view, and hence the effective radius of the rim r_o was taken as the geometric mean of r_o^S and r_o^B . The geometric mean is indicated by the dashed line in Fig. 10.

The corrugation of the rim following impact has been attributed by various investigators to the Rayleigh–Plateau instability, the Rayleigh–Taylor instability, the Kelvin–Helmholtz instability, the Ritchmyer–Meshkov instability,

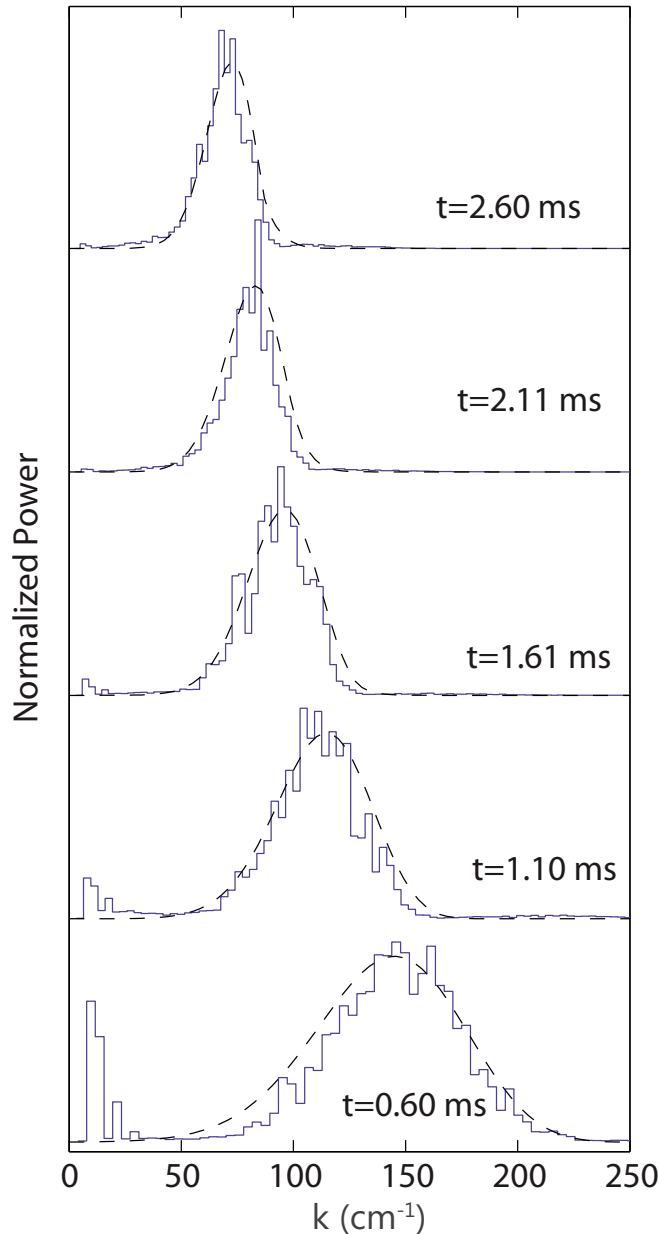


FIG. 8. (Color online) Normalized power spectra vs wavenumber for various times after impact for parameter set number 1. The solid curve is the average of multiple experiments and the dashed curve is the prediction from the Rayleigh–Plateau model. The peaks at low wavenumber arise from digitization effects and small nonparallelism of the camera sensor and the impact plane; for example, the largest of these peaks corresponds to the $m=2$ mode.

and nonlinear amplification. Given the vast range of splash morphologies, it may be that each of these effects are dominant in some particular parameter regime. In the following two sections, we compare our measurements in the limited parameter regime labeled *Crown Droplets*, and to some extent the parameter regime at lower Re number, to each of these mechanisms.

IV. RAYLEIGH–PLATEAU INSTABILITY

We compared our measurements to a theoretical calculation based on the physical idea that the rim behaves like a cylinder of fluid subject to surface tension forces. Such a

cylinder is unstable to perturbations whose wavelengths are greater than 2π times the radius of the cylinder. This so-called Rayleigh–Plateau instability accounts for the decay of cylindrical jets into droplets.²³ If the jet is subject to a broad spectrum of initial perturbations, the typical drop size is set by the wavelength of the perturbation that has the highest growth rate. A characteristic feature of the instability is that this “Rayleigh” mode is a multiple of the radius of the cylinder. In our calculation, we assume that the attachment of the sheet to the rim is negligible. We also treat the cylinder as straight, which is a good approximation if, as in our experiments, the unperturbed rim radius $r_o(t)$ is much smaller than the rim’s radial distance from the impact center $R(t)$.

To perform a linear stability analysis, the local rim radius $r(\theta, t)$ is written as

$$r(\theta, t) = r_o(t) + \epsilon(\theta, t), \quad (1)$$

where θ is the angle as seen from the center, and ϵ is a small perturbation to the mean radius. The overwhelming majority of past studies focused on the growth of a single mode. Instead, we consider a spectrum of modes in order to characterize the randomness of the perturbations growing on the rim. Thus as an initial perturbation we take the spectral decomposition

$$\epsilon(\theta, 0) = \sum_{m=-N}^N a_m e^{im\theta}. \quad (2)$$

In our model, the initial amplitude of each mode a_m is set equal to the same constant a_0 for all values of m . This is equivalent to assuming that the initial spectrum is flat.

We start from the classical result for the growth rate of perturbations on a cylinder of constant radius with no flow inside the cylinder. The growth rate σ_m of the m th mode is determined implicitly by

$$\begin{aligned} 2x^2(x^2 + y^2) \frac{I_1'(x)}{I_0(x)} \left[1 - \frac{2xy}{x^2 + y^2} \frac{I_1(x) I_1'(y)}{I_1(y) I_1'(x)} \right] - x^4 + y^4 \\ = \frac{\gamma r_o x I_1(x)}{\rho \nu^2 I_0(x)} (1 - x^2). \end{aligned} \quad (3)$$

Here $x = k_m r_o$, $k_m = m/R$ is the wavenumber of the m th mode, $y^2 = x^2 + \sigma_m^2 r_o^2 / \nu$, and I_n are modified Bessel functions of the first kind.³⁰ As explained in Eggers and Villermaux,³¹ we expand on this result to include (a) the growth of the rim as it entrains the sheet and (b) the stretching of the rim as the sheet expands. According to Eq. (106) of Eggers and Villermaux,³¹ the time evolution of the perturbation in the presence of (a) and (b) is given by

$$\frac{d \ln \epsilon(\theta, t)}{dt} = -\frac{s}{2} + \sigma_m, \quad (4)$$

where s is the stretch rate due to the expansion of the rim. In other words, longitudinal stretching always *decreases* the amplitude of the perturbation,³¹ since it causes fluid elements to contract in the radial direction. The growth rate σ_m is calculated from the classical theory with no stretching or flow into the cylinder [i.e., Eq. (3)]. This approximation is justified by the fact that the base state changes according to a

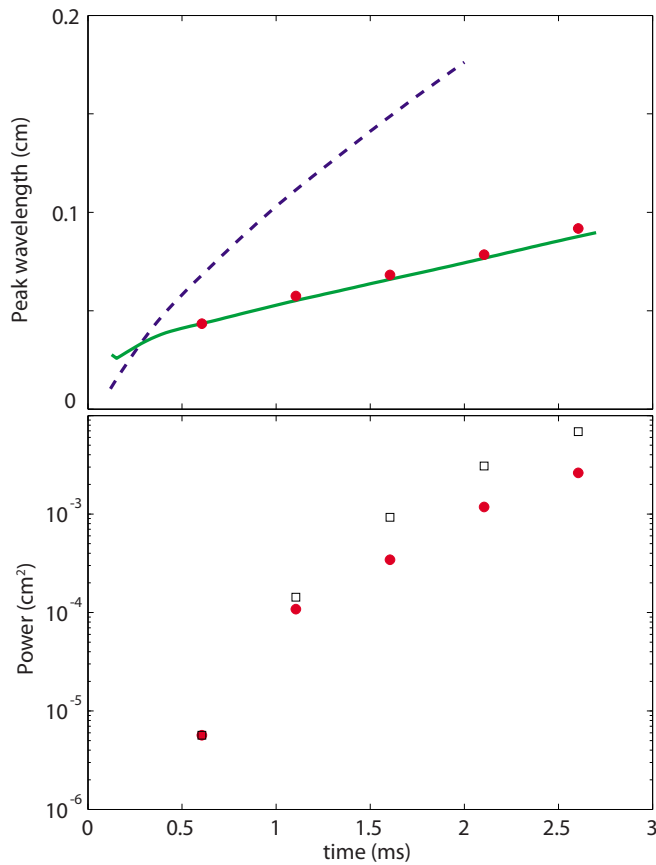


FIG. 9. (Color online) Peak wavelength (top) and power (bottom) vs time: measured (circles) and the predicted values from the Rayleigh–Plateau (solid line, squares) and the Rayleigh–Taylor (dashed line) models for parameter set number 1.

linear law (see Fig. 10), while the growth of perturbations is exponential, and thus faster. Indeed, while the rim radius changes by a factor of 4 between 0.5 and 2.5 ms (see Fig. 10), the amplitude of the perturbation changes by more than a decade in the same time span (see Fig. 9).

Since the stretch rate is $s = \dot{R}/R$, Eq. (4) can be integrated in time to give

$$\ln \frac{\epsilon(\theta, t)}{\epsilon(\theta, 0)} = -\frac{1}{2} \ln \frac{R(t)}{R(0)} + \int_0^t dt' \sigma_m. \quad (5)$$

Using the initial perturbation (2), we then obtain

$$r(\theta, t) = r_o + \sqrt{\frac{R(0)}{R(t)}} \sum_{m=-N}^N a_m \times \exp \left\{ im\theta + \int_0^t dt' \sigma_m [k_m = m/R(t), r_o(t)] \right\}. \quad (6)$$

The spectra obtained from our calculation are compared in Fig. 8 to those obtained from our most precise experiments. We find excellent agreement in both the position and width of the central peak. Note that the peak position moves to lower wavenumbers as time goes on, since the original perturbation is stretched out as $R(t)$ increases and $r_o(t)$ swells. The peak width decreases in time as the most unstable wavenumber “Rayleigh mode” is amplified more

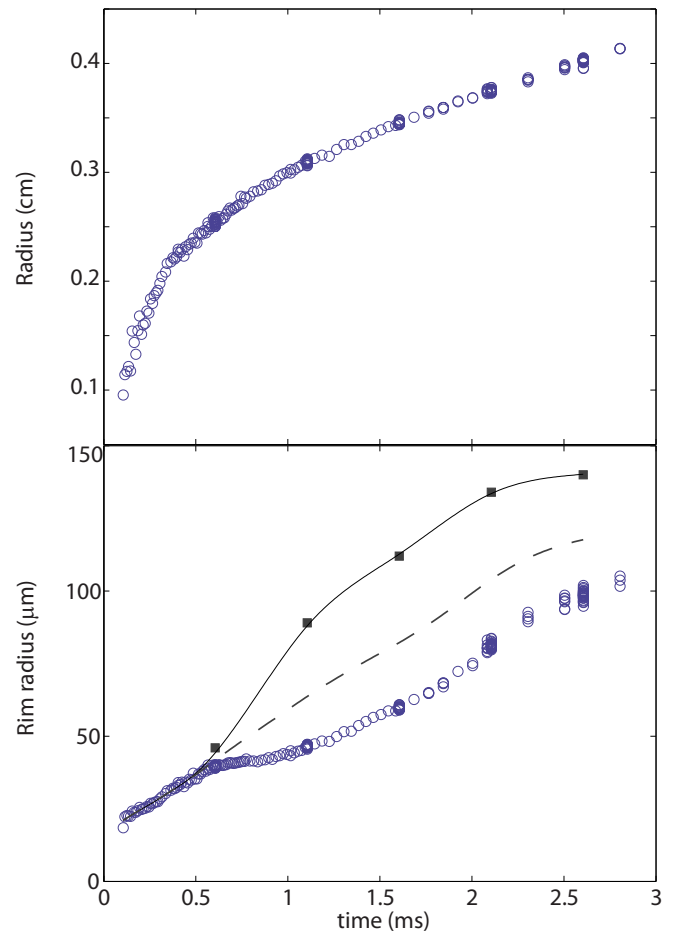


FIG. 10. (Color online) Horizontal distance of the rim from the impact center (top) and radius of the rim (bottom) measured from below (circles) and from side (squares) vs time for parameter set number 1. The solid line is a cubic spline of the side data and the dashed line is the geometric mean of the rim radius r_o .

strongly than the wavenumbers surrounding it, and thus dominates the spectrum more and more. The theoretical peak wavenumber is obtained by fitting the calculated spectra with a Gaussian. The peak wavenumber at any given instant t , defined as the mode with the most power, is determined by not only the instantaneously most rapidly growing mode but also by the history of the other modes. Thus the peak wavelength is given by the maximum of $\exp\{\int_0^t dt' \sigma_m(t')\}$. A comparison of these data with experiments is shown in Fig. 11. The calculation reproduces the measured wavelength to within $\pm 10\%$ for all our experiments and to within $\pm 5\%$ for our most precise experiments at $\text{Re}=1060$, $\text{We}=760$, and $\text{H}^*=0.20$. It bears emphasizing that the calculation of the peak position and width depends only on the experimentally determined variables $r_o(t)$ and $R(t)$, i.e., there are no adjustable parameters.

Our results also account for irregularities in the pattern. Under the action of the Rayleigh–Plateau instability, perturbations away from the most unstable wavelength are amplified as well, albeit at a smaller rate. As shown in Fig. 8, the width of the spectrum evolved by our equations from initial white noise spectrum is equivalent to that of our data. Thus the irregularity is governed by the width of the central peak

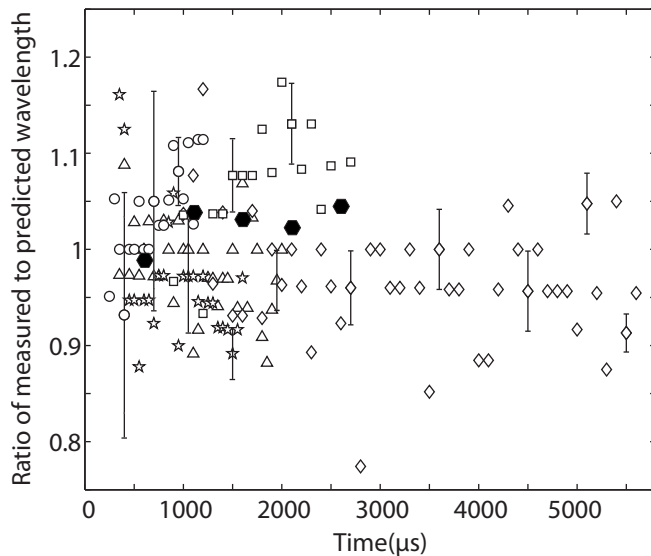


FIG. 11. Ratio of measured to theoretically expected peak wavelength vs time for the Rayleigh–Plateau model for all experiments: number 1 (hexagons), number 2 (circles), number 3 (stars), number 4 (diamonds), number 5 (squares), and number 6 (triangles). Note that the most accurate data are for parameter set number 1.

of the spectrum, a phenomenon which to our knowledge has never been considered quantitatively for the Rayleigh–Plateau instability.³¹ Instead, typical measurements of linear instability impose a wavelength from the outside so as to produce a regular pattern, and irregularity is often attributed to nonlinear effects.

The theoretical peak power was obtained by fitting the calculated power spectra to a Gaussian. The overall scale of these data is determined by the initial amplitude a_0 . This parameter was chosen such that theory and experiment agree at $t=0.6$ ms. These data are compared to experiments in Fig. 9. The agreement between the theoretical and measured maximum power is fair, showing a systematic overestimate of the actual growth rate. We believe the deviations arise from both experimental and modeling issues. On the experimental side, our measurements of the amplitude from below undervalue the actual amplitude because we measure its projection on the horizontal plane. On the theoretical side, the assumption in our model that the rim is cylindrical and the unstable mode is varicose may contribute to the disagreement. First, even if the sheet is thin compared to the rim radius, the attachment constrains the evolution of the rim and the reduction of surface energy due to corrugation is not as great as it would be for an unconstrained cylinder. A model calculation in which the curve along which the sheet attaches to the rim is kept uncorrugated (i.e., straight), as observed experimentally, shows that the growth rate decreases. Second, the gradual transition from rim to sheet will slow the growth of the instability. For example, in the extreme case in which the rim is simply a semicircular end of the sheet, there is no surface energy to be gained from a local reduction of the rim radius, and thus no instability at all.

V. OTHER MECHANISMS

A. Rayleigh–Taylor instability

Mechanisms based on the Rayleigh–Taylor instability posit that the generation of secondary droplets arises from the deceleration of the sheet. Krechetnikov and Homsy²² have argued for this mechanism based on their experiments conducted with milk. Here we show that the Rayleigh–Taylor mechanism predicts wavelengths significantly greater than those observed experimentally. This prediction is based on direct measurements of the acceleration of the rim.

The driving force for the Rayleigh–Taylor instability comes from the deceleration of a fluid surface relative to a less dense external medium, in our case air (whose density can be neglected). It is opposed by surface tension, which favors a flat interface. As a result, the characteristic length scale governing this instability is the effective “capillary length”

$$\ell_a = \sqrt{\frac{\gamma}{\rho a}} \quad (7)$$

based on the deceleration a . If ℓ_a is greater than the rim radius r_0 , inertial effects are small at the length scales relevant to our study.

We compute the Bond number $\text{Bo}^{-1} = \ell_a^2 / r_0^2$ using the deceleration measured by fitting the vertical and horizontal components of position and differentiating the result twice with respect to time. The deceleration and the Bond number are plotted in Fig. 12. These data show that over the time interval for which we observe growth of perturbations along the rim, ℓ_a is indeed far greater than r_0 , confirming that the effect of acceleration is unimportant.

The same conclusion can also be drawn directly from the dispersion relation for the Rayleigh–Taylor instability of a flat interface, for which the growth rate σ_m is defined implicitly by Chandrasekhar³⁰

$$\sigma_m^2 = ak \left(1 - \frac{k^2 \gamma}{\rho \nu} \right) - 4k^2 \nu [\sigma_m + k \nu (\sqrt{k^2 + \sigma_m^2 / \nu} - k)]. \quad (8)$$

The cutoff wavenumber, above which no amplification takes place, is $1/\ell_a$. The most amplified wavenumber is slightly smaller (corresponding to a longer wavelength), but its precise value depends on the viscosity. Using the acceleration shown in Fig. 12, the peak wavelength as predicted by Eq. (8) is plotted in Fig. 9. At $t \approx 250$ μs the peak wavelengths coincide, but thereafter the Rayleigh–Taylor prediction is in increasing disagreement with the experimental results, consistent with our expectations based on the Bond number.

The rim of the sheet is curved, not flat, as assumed in the derivation of Eq. (8). However, as argued by Krechetnikov,³² this only weakens the Rayleigh–Taylor instability, and shifts the range of unstable wavenumbers to even smaller values, or equivalently to higher wavelengths. In other words, the dashed line shown in Fig. 9 is only a *lower bound* for the true peak wavelength of the Rayleigh–Taylor instability. The physical reason is that if the heavy fluid is bounded by a *convex* interface, the mass of fluid being accelerated is less than that for a flat interface. Since the Rayleigh–Taylor in-

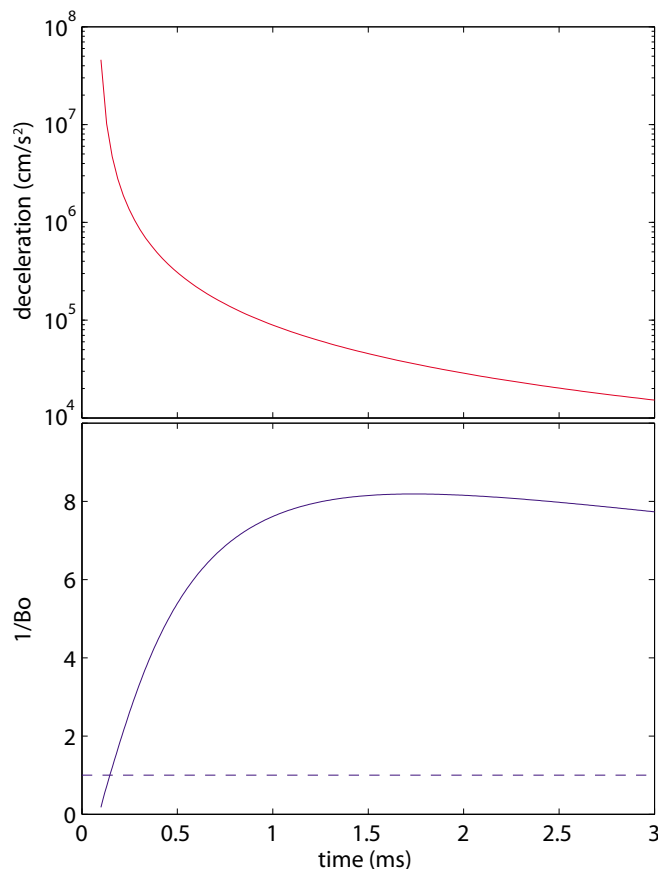


FIG. 12. (Color online) Deceleration (top) measured from the trajectory of the rim and inverse Bond number (bottom) vs time. For most of the splash inverse Bond number is large compared to one, indicating the dominant role of capillarity over inertial forces.

stability is inertia-driven, it becomes less effective. To make up for the loss of mass, the wavelength in the direction along the rim has to be even greater than expected on the basis of Eq. (8).

Even more recently, the same point has been expanded upon in Krechetnikov³³ by performing a linear stability calculation about a fluid cylinder of circular cross section, which is accelerated in a direction normal to its axis. It is claimed that the interplay between the Rayleigh–Plateau and Rayleigh–Taylor instabilities leads to a change in the dispersion relation. The problem with the calculation of Krechetnikov³³ is that a hydrostatic pressure gradient will build up inside the cylinder, which deforms its equilibrium state from a circular cross section to a new deformed base state. The linear stability calculation thus is not performed about the true equilibrium state of the system, which leads to inconsistencies. For example, the dispersion relation reported in Krechetnikov³³ shows instability at zero wavenumber, corresponding to an exponential time dependence of the base state. But as argued above, the fluid cylinder will merely relax to a new equilibrium state when accelerated. We hasten to add, though, that none of these effects are of importance for the present experiments, since the Bond number is small.

B. Richtmyer–Meshkov instability

Gueyffier and Zaleski²⁸ present simulations in which the length of fingers on the rim grow linearly in time. They interpret this result as evidence for a Richtmyer–Meshkov instability triggered by the impulsive impact of the drop on the substrate. Our experiment addresses a much earlier regime, during which the amplitude of perturbations is much smaller than the width of the rim. We find exponential growth for this initial regime, whereas a Richtmyer–Meshkov instability is expected to grow linearly in time. Krechetnikov and Homsy²² also argue for the Richtmyer–Meshkov instability, based on the experimental observation that the instability occurs in the very early stages of impact, but their experiments were conducted with a non-Newtonian fluid and for $Re \approx 3000$, $We \approx 1000$ which, if the fluid was Newtonian, would correspond to the highly irregular splashes we observe in the crown droplet/microdroplet regime.

C. Nonlinear instabilities

Yarin and Weiss¹⁴ proposed a nonlinear amplification mechanism governed by the eikonal equation. This mechanism does not select a particular wavelength but rather sharpens pre-existing perturbations of finite amplitude. Our measurements of the power spectrum show a clear wavelength and thus are inconsistent with this prediction.

VI. DISCUSSION AND CONCLUSION

Other investigators reached the same conclusions as ours. Bremond and Villermaux²⁷ found that the Rayleigh–Plateau instability accounts for the fragmentation of the lamella produced by colliding jets. Our results are also consistent with numerical simulations of Rieber and Frohn.²⁶

Our results do not agree with those of Yarin and Weiss¹⁴ who found a discrepancy between the expected and measured number of ejected droplets. We suspect that differences in the experimental conditions account for the disagreement as their experiments were conducted at a high repetition rate (up to 15 000 Hz) in which the liquid layer was highly perturbed by the previous impact. Our results are also at odds with the work of Fullana and Zaleski,²⁵ who use numerical simulations as well as theoretical arguments very similar to ours to conclude that the Rayleigh–Plateau instability does not produce sufficient growth to lead to the breakup of the rim. However, no justification is given for their choice of parameter values. In addition, the total length of the sheet simulated by Fullana and Zaleski²⁵ was only 40 times the thickness of the sheet, and thus permitted to follow the rim evolution only over a limited period of time. Our calculation, by contrast, is based on parameter values obtained directly from experiment, and leads to order one perturbations of the rim over the time the sheet retracts. Thus Fullana and Zaleski’s conclusions are invalidated for the experimental parameter regime studied by us.

In conclusion, we study the crown splash regime of the impact of a drop onto a thin film. This permits us to follow the growth of the symmetry-breaking instabilities from very small values through significant perturbations of the rim,

leading to the formation of droplets. For a wide range of parameters in this regime, we show (i) that there is a well-defined wavelength selection process, (ii) that the amplification of the selected modes is consistent with a linear instability, and (iii) that the maximum number of secondary droplets is determined by the most unstable wavelength. Our measurements of the most unstable wavelength are in excellent agreement with a model based on the Rayleigh–Plateau instability. Hence, the number of incipient secondary droplets is proportional to the circumference of the splash sheet divided by the most unstable wavelength (and therefore proportional to the radius of the rim), and the irregularity of the crown is set by amplification of random noise by the spectrum of growth rates of the Rayleigh–Plateau instability.

ACKNOWLEDGMENTS

We thank Daniel Bonn for comments on the manuscript and Christophe Josserand for discussions. R.D.D. acknowledges support from the James S. McDonnell Foundation 21st Century Science Initiative in Studying Complex Systems-Research Award.

- ¹D. T. Ho, W. E. Asher, L. F. Bliven, P. Schlosser, and E. L. Gordan, “On mechanisms of rain-induced air-water gas exchange,” *J. Geophys. Res.* **105**, 24045, doi:10.1029/1999JC000280 (2000).
- ²M. Pasandideh-Fard, S. D. Aziz, S. Chandra, and J. Mostaghimi, “Cooling effectiveness of a water drop impinging on a hot surface,” *Int. J. Heat Fluid Flow* **22**, 201 (2001).
- ³D. Bartolo, C. Josserand, and D. Bonn, “Singular jets and bubbles in drop impact,” *Phys. Rev. Lett.* **96**, 124501 (2006).
- ⁴M. R. O. Panão and A. L. N. Moreira, “Flow characteristics of spray impingement in PFI injection systems,” *Exp. Fluids* **39**, 364 (2005).
- ⁵R. D. Deegan, P. Brunet, and J. Eggers, “Complexities of splashing,” *Nonlinearity* **21**, C1 (2008).
- ⁶A. M. Worthington and R. S. Cole, “Impact with a liquid surface, studied by the aid of instantaneous photography,” *Philos. Trans. R. Soc. London, Ser. A* **189**, 137 (1897).
- ⁷A. M. Worthington and R. S. Cole, “Impact with a liquid surface studied by the aid of instantaneous photography. Paper II,” *Philos. Trans. R. Soc. London, Ser. A* **194**, 175 (1900).
- ⁸A. L. Yarin, “Drop impact dynamics: Splashing, spreading, receding, and bouncing,” *Annu. Rev. Fluid Mech.* **38**, 159 (2006).
- ⁹H. E. Edgerton, *Stopping Time: The Photographs of Harold Edgerton* (Abrams, New York, 1977).
- ¹⁰F. E. C. Culick, “Comments on a ruptured soap film,” *J. Appl. Phys.* **31**, 1128 (1960).
- ¹¹G. Taylor, “The dynamics of thin sheets of fluid. III. Disintegration of fluid sheets,” *Proc. R. Soc. London, Ser. A* **253**, 313 (1959).
- ¹²R. F. Allen, “The mechanics of splashing,” *J. Colloid Interface Sci.* **124**, 309 (1988).
- ¹³S. Chandra and C. T. Avedisian, “On the collision of a droplet with a solid surface,” *Philos. Trans. R. Soc. London, Ser. A* **432**, 13 (1991).
- ¹⁴A. L. Yarin and D. A. Weiss, “Impact of drops on solid surfaces, self-similar capillary waves, and splashing as a new type of kinematic discontinuity,” *J. Fluid Mech.* **283**, 141 (1995).
- ¹⁵C. Mundo, M. Sommerfeld, and C. Tropea, “Droplet-wall collisions: Experimental studies of the deformation and breakup process,” *Int. J. Multiphase Flow* **21**, 151 (1995).
- ¹⁶G. E. Cossali, A. Coghe, and M. Marengo, “Impact of a single drop on a wetted solid surface,” *Exp. Fluids* **22**, 463 (1997).
- ¹⁷H. Fujimoto, S. Ito, and I. Takezaki, “Experimental study of successive collision of two water droplets with a solid,” *Exp. Fluids* **33**, 500 (2002).
- ¹⁸L. J. Leng, “Splash formation by spherical drops,” *J. Fluid Mech.* **427**, 73 (2001).
- ¹⁹S. T. Thoroddsen, “The ejecta sheet generated by the impact of a drop,” *J. Fluid Mech.* **451**, 373 (2002).
- ²⁰G. E. Cossali, M. Marengo, A. Coghe, and S. Zhdanov, “The role of time in single drop splash on thin film,” *Exp. Fluids* **36**, 888 (2004).
- ²¹I. V. Roisman, T. Gambaryan-Roisman, O. Kyriopoulos, P. Stephan, and C. Tropea, “Breakup and atomization of a stretching crown,” *Phys. Rev. E* **76**, 026302 (2007).
- ²²R. Krechetnikov and G. M. Homsy, “Crown-forming instability phenomena in the drop splash problem,” *J. Colloid Interface Sci.* **331**, 555 (2009).
- ²³L. Rayleigh, “On the instability of jets,” *Proc. London Math. Soc.* **4**, 10 (1878).
- ²⁴A. M. Worthington, “On the spontaneous segmentation of a liquid annulus,” *Proc. Phys. Soc. London* **30**, 49 (1879).
- ²⁵J. M. Fullana and S. Zaleski, “Stability of a growing end rim in a liquid sheet of uniform thickness,” *Phys. Fluids* **11**, 952 (1999).
- ²⁶M. Rieber and A. Frohn, “A numerical study on the mechanism of splashing,” *Int. J. Heat Fluid Flow* **20**, 455 (1999).
- ²⁷N. Bremond and E. Villermaux, “Atomization by jet impact,” *J. Fluid Mech.* **549**, 273 (2006).
- ²⁸D. Gueyffier and S. Zaleski, “Finger formation during droplet impact on a liquid film,” *C.R. Acad. Sci., Ser. IIC: Chim* **326**, 839 (1998).
- ²⁹L. Xu, W. W. Zhang, and S. R. Nagel, “Drop splashing on a dry smooth surface,” *Phys. Rev. Lett.* **94**, 184505 (2005).
- ³⁰S. Chandrasekhar, *Hydrodynamic and Hydromagnetic Stability* (Dover, New York, 1981).
- ³¹J. Eggers and E. Villermaux, “Physics of liquid jets,” *Rep. Prog. Phys.* **71**, 036601 (2008).
- ³²R. Krechetnikov, “Rayleigh–Taylor and Richtmyer–Meshkov instabilities of flat and curved interfaces,” *J. Fluid Mech.* **625**, 387 (2009).
- ³³R. Krechetnikov, “Stability of liquid sheet edges,” *Phys. Fluids* **22**, 092101 (2010).